Decisions and Trade-Offs in the Design of a Mass Spectrometer for Jupiter's Icy Moons

Davide Lasi
University of Bern, Physics Institute
Sidlerstrasse 5
Bern, CH-3012 (Switzerland)
davide.lasi@space.unibe.ch

Stefan Meyer
University of Bern, Physics Institute
Sidlerstrasse 5
Bern, CH-3012 (Switzerland)
stefan.meyer@space.unibe.ch

Daniele Piazza
University of Bern, Physics Institute
Sidlerstrasse 5
Bern, CH-3012 (Switzerland)
daniele.piazza@space.unibe.ch

Mathias Lüthi
University of Bern, Physics Institute
Sidlerstrasse 5
Bern, CH-3012 (Switzerland)
luethi@space.unibe.ch

Andreas Nentwig
University of Bern, Physics Institute
Sidlerstrasse 5
Bern, CH-3012 (Switzerland)
andreas.nentwig@space.unibe.ch

Mario Gruber
University of Bern, Physics Institute
Sidlerstrasse 5
Bern, CH-3012 (Switzerland)
mario.gruber@space.unibe.ch

Stefan Brüngger
University of Bern, Physics Institute
Sidlerstrasse 5
Bern, CH-3012 (Switzerland)
stefan.bruengger@space.unibe.ch

Michael Gerber
University of Bern, Physics Institute
Sidlerstrasse 5
Bern, CH-3012 (Switzerland)
michael.gerber@space.unibe.ch

Saverio Braccini
University of Bern, LHEP
Sidlerstrasse 5,
Bern, CH-3012 (Switzerland)
saverio.braccini@lhep.unibe.ch

Marek Tulej
University of Bern, Physics Institute
Sidlerstrasse 5
Bern, CH-3012 (Switzerland)
marek.tulej@space.unibe.ch

Martina Föhn
University of Bern, Physics Institute
Sidlerstrasse 5
Bern, CH-3012 (Switzerland)
martina.foehn@space.unibe.ch

Peter Wurz
University of Bern, Physics Institute
Sidlerstrasse 5
Bern, CH-3012 (Switzerland)
peter.wurz@space.unibe.ch

Abstract—**This paper describes the Neutral gas and Ion Mass spectrometer (NIM) onboard ESA's JUpiter ICy moon Explorer (JUICE). Instead of detailing the nuts and bolts of the design, we recount it in terms of 'given', architectural, and design decisions. 'Given' decisions are relative to elements of the instrument defined at the outset of the project, which bound the solution space to be explored by the development team. These decisions comprise the definition of the instrument concept (time-of-flight), sample ionization, MCP detector, ion optics technology, radiation shielding, and allocation of electronics' functions. Architectural and design decisions regard other elements of the instrument defined during the preliminary and detailed design phases, after trade-offs accounting for both technical and programmatic factors. These decisions regard the instrument's ion source, mechanism, FPGA, emitters, PCB interconnect, detector, materials, circuitry of the emission controller and high-voltage pulser, and software. Lessons learned are discussed throughout, including decisions that, ex-post, should have been made differently. This recollection ends with the first mass spectrum acquired with the flight model.**

TABLE OF CONTENTS

978-1-7821-2734-7/20/$31.00 ©2020 IEEE

1. INTRODUCTION

This paper describes the Neutral gas and Ion Mass Spectrometer (NIM) of the Particle Environment Package (PEP) onboard ESA's JUpiter ICy moons Explorer (JUICE) [1]. In particular, this work interprets the development of the instrument in terms of decisions and trade-offs made to meet the ambitious science goals of the mission in the extreme environment of Jupiter (radiation), subject to tight resources (mass and power) and programmatic constraints.

The design of the instrument is recounted in terms of 'given', architectural, and design decisions. These include decisions about the instrument's sensor, electronics, software, and radiation shielding. This recollection ends with the first mass spectra acquired with the Proto-Flight Model (PFM).

We believe that this approach to recounting the development of the instrument in terms of decisions and trade-offs does a better service to the future generations of designers of space mass spectrometers than a mere description of the nuts and bolts of the final design. By telling not only the path that we followed but also the pattern of alternatives that we dropped, and why, we aim to provide a useful material that can inform the development of future similar instruments.

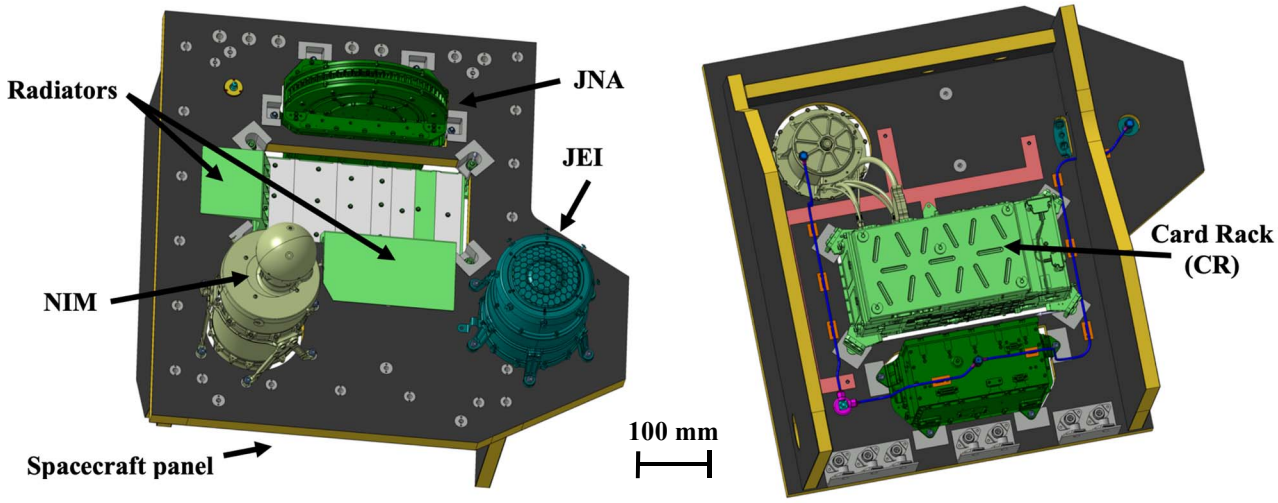

Figure 1 Overview of the Particle Environment Package (PEP) Nadir Unit (NU), including the Neutral gas and Ion Mass spectrometer (NIM), the Jovian Neutrals Analyzer (JNA) and the Jovian Electron and Ion analyzer (JEI) as of 2019.

2. Context

NIM is a Time-Of-Flight Mass Spectrometer (TOF MS) selected in 2013 for the ESA mission JUICE. The mission comprises multiple flybys of Jupiter's icy moons Europa, Callisto, and Ganymede and a final orbital phase around Ganymede. NIM is one of six instruments of PEP [2], which comprises four units. The PEP Nadir Unit (NU, Figure 1), where NIM is located, is accommodated on the nadir plane of the spacecraft (Figure 2).

The instrument is the 4th generation of TOF MS for application on a spacecraft developed by the University of Bern, after RTOF for ESA's Rosetta [3], P-BACE [4], and NGMS for Roscosmos' Luna-Resurs [5] [6]. The development of NIM benefited particularly from the latter, thanks to a partial overlap in time and team composition. Table 1 summarizes the key milestones of the project. The team comprised eight engineers (mechanics, electronics, FGPA, software), two modelers (structural, thermal), a senior scientist, about four technicians, a Ph.D. student, a project manager, and the PI.

The development of NIM presented several challenges. First, it took place in the context of a multi-instrument suite, for complex technical interfaces and programmatic dependencies of a 'team of teams.' Second, it had to address new issues related to the operation of a TOF MS in the Jupiter radiation environment (Figure 3), such as energetic electron detection efficiencies of Micro-Channel Plates. The Galileo dust detector [7], also a TOF instrument, had a different architecture, and the development of MASPEX [8], a TOF MS for NASA's Europa Clipper, was substantially concurrent with NIM's, and therefore faced similar challenges at about the same time. Finally, the instrument's design space was constrained by a number of risk-mitigation requirements from the JUICE project office put in place to mitigate risk of the first large-class mission and the first mission to Jupiter of the European Space Agency (ESA).

Table 1 Summary of key project dates.

Event	Year
Instrument proposal accepted (initiation)	2013
Requirements Review	2014
Preliminary Design Review (PDR)	2017
Critical Design Review (CDR)	2018
Proto-Flight Model delivery	2020
Launch	2022

3. Goals and Requirements

NIM is conceived to address the science goals of JUICE related to the understanding of the neutral exospheric and ionospheric composition and structure of Europa, Ganymede, and Callisto. Specifically, NIM will measure neutrals and ions in the exospheres of these icy moons during the early-mission's flybys (> 200–400 km altitude at closest approach)

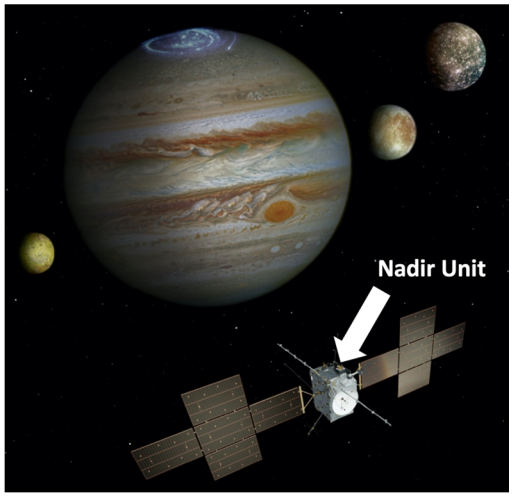

Figure 2 Location of the PEP Nadir Unit on the JUICE spacecraft (Credits: ESA and Airbus Defence and Space).

and the late-mission orbits around Ganymede (> 200–500 km altitude). The required spatial resolution is ~25–50 km.

The L3 instrument requirements are summarized in Table 2. They are derived from L1 science and L2 measurement requirements considering the spacecraft velocity (~4–7 km/s for flybys and ~2 km/s for Ganymede orbits) and the expected exospheric concentration from modeling ([9], [10], [11]).

These requirements defined the problem space to be addressed by the team. Although they may appear to be easily achievable for a state-of-the-art instrument, fulfilling them *within the allocated power and mass and in the Jovian radiation environment* (Figure 3) was the main challenge.

Table 2 Key instrument requirements.

Requirement	Value	Unit
Mass range	≥ 300	u
Mass resolution (M/ΔM, below 100u)	≥ 500	–
Measurement cadence	≥ 5*	s
Dynamic range (for 5s spectra)	≥ 10^5	–
Mass (instrument + shielding)	<3+3	kg
Power (before common DCC)	≤ 12	W
Data allocation (whole mission)	~2	GB

4. METHODS

We refer in this paper to three categories of decisions to recount the instrument development: 'given', architectural, and design decisions.

'Given' decisions denotes the choices about the system architecture or design made at the outset of the project or during the lengthy 'shaping phase' [12] preceding the formal initiation of the project. We defined this category of decision to distinguish what was an input to the development work (the 'given' decisions) and what its output (the architectural and design decisions). For NIM, some of the 'given' decisions resulted from incentives to use heritage and high-TRL solutions (legacy decisions), whereas other ones were made from reasonable evidence that they are the best or only solutions to meet the JUICE science goals, subject to the mission profile and technical and programmatic constraints. The qualifier 'given' highlights the fact that these decisions limited upfront the span of the solution space that the team could explore, and not much work was made by the team to explore alternative solutions. Moreover, it emphasizes their stability, in that they were never called into question later on (with one exception due to a late-test failure).

Architectural and design decisions indicate the choices made during preliminary (Phase B) and detailed (Phase C) design of the instrument after technical and programmatic trade-offs.

Architectural decisions regard the system's form and function, and ought to be made early on because it is hard to change them afterward [13]. Often, they are made under uncertainty, because there are not enough resources to gain sufficient information (e.g., through prototyping and testing).

Design decisions are relative to more specific details about the system or subsystems that often makes sense to address only after having taken other architectural decisions. These decisions are the outcome of in-depth engineering work by a mature project team, and they typically depend on the results of modeling, prototyping, and experiments. Some of these decisions can be postponed to grain more information, as long as they are not on the critical path.

In the course of a system's development that spans over several years, hundreds of decisions are made, and the task of summoning them may look daunting. We follow the 'magic number seven, plus or minus two' [14], to keep this list short and draw attention to the few decisions that mattered the most in the development of NIM.

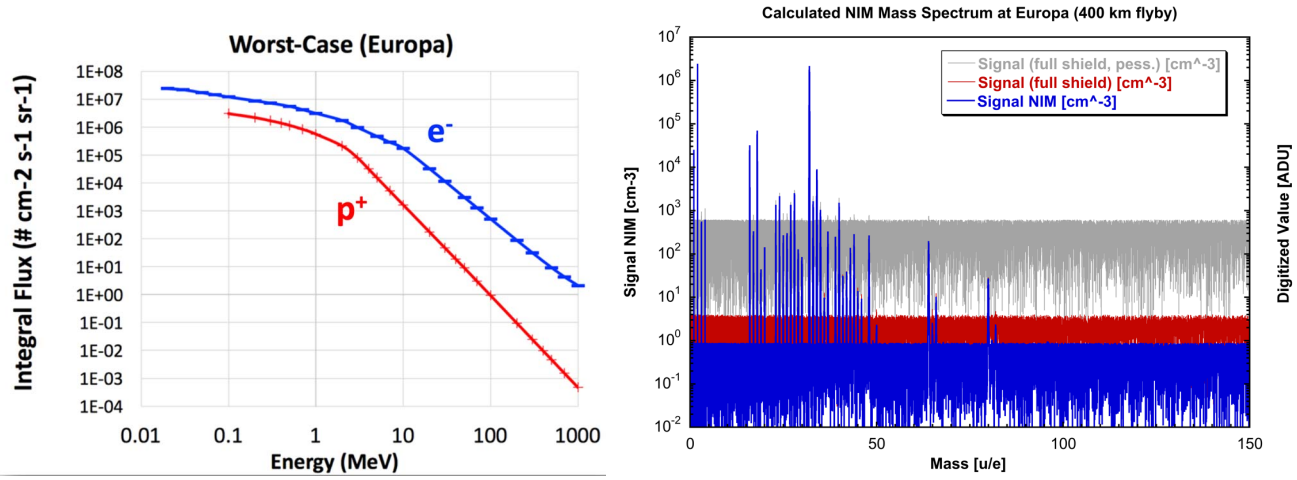

Figure 3 Left: radiation environment at Europa (sizing case for NIM). Right (reproduced from [22]): blue, calculated NIM calibrated mass spectrum at Europa for a flyby at an altitude of 400 km; gray, radiation background in absence of shielding; red, radiation background after shielding. Accumulation time: 5 s, repetition rate: 10 kHz.

Throughout the paper, we occasionally use the formalism of Object Process Methodology (OPM). Just knowing that 'ovals' represent processes and 'boxes' represents objects (instruments or operands of processes) is sufficient to understand the diagrams reported here. The appreciation of the finer details of these representations are left to the interested reader, to whom we suggest the recent ISO Standard ISO/PAS 19450:2015 as a handy reference and introduction to OPM.

5. 'GIVEN' DECISIONS

The following decisions about the instrument are considered to be 'given' because they had been already made by the time the project officially started in 2013, during the early study phase, or were made very soon after the project's initiation:

G1. The instrument be a reflectron TOF MS.

G2. The ionization of neutrals be via electron impact.

G3. The detector be a Micro-Channel Plate (MCP).

G4. The mass analyzer be based on the same ceramic ion optics construction successfully flown on previous missions and be unshielded from radiation.

G5. The instrument electronics be shielded from radiation by a common vault (Card Rack) shared with other PEP instruments, and the mass analyzer be exposed to radiation, except for the shielded detector.

G6. The instrument be interfaced to the spacecraft via primary Direct Current Converters (DCC) and a Data Processing Unit (DPU), provided by other PEP teams in Finland and Hungary and shared with other PEP instruments from Sweden and Germany.

G7. The control of the instrument and the processing of the data it generates (science and housekeeping) be via an application software model running on the common DPU, whereas the high-speed data processing and time-critical functions be performed by the NIM electronics using an FPGA.

These decisions, all architectural, limited the solution space that could answer the problem space set forth by the requirements in Table 2. They nailed down many key aspects of the architecture, as the Level 1 decomposition in Figure 4 and the functional architecture representation in Figure 5 show. Yet, making these decisions early on was necessary to start several lengthy design, procurement, manufacturing, and qualification tasks.

Decision About the Mass Analyzer (G1–G4)

The TOF MS architecture (G1) was selected for its superior capability of meeting the science requirements compared to alternatives, such as a quadrupole MS. Indeed, a TOF MS can

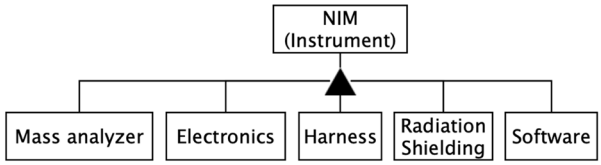

Figure 4 NIM Level 1 Decomposition.

achieve a dynamic range of ~2–3 decades on a single shot spectrum recorded in few μs that cover a broad mass range of >300 u. These spectra are then integrated into a histogram that is the ultimate science result (Figure 5). Working at a repetition rate of 10 kHz, a TOF MS can achieve a dynamic range of ~5–6 decades for integration time of the order of ~1–10 s. Thus it can offer quantitative analysis of samples with many and unevenly concentrated species, while providing a good spatial profiling along the trajectory of the spacecraft.

A quadrupole MS may would perform the same measurement by scanning the mass range and implementing gain switching to achieve the same or better sensitivity. But during the scanning, the sample concentration and composition may vary significantly (the exospheric column height has an exponential profile). Yet, a proper implementation of gain switching and the precise knowledge of the gain at every moment for a quantitative measurement is a major engineering challenge. These properties of a quadrupole MS make it less desirable than a TOF for a mission profile like JUICE's, because a TOF MS acquires spectra with the same gain across the whole m/z range at high repetition rate (kHz).

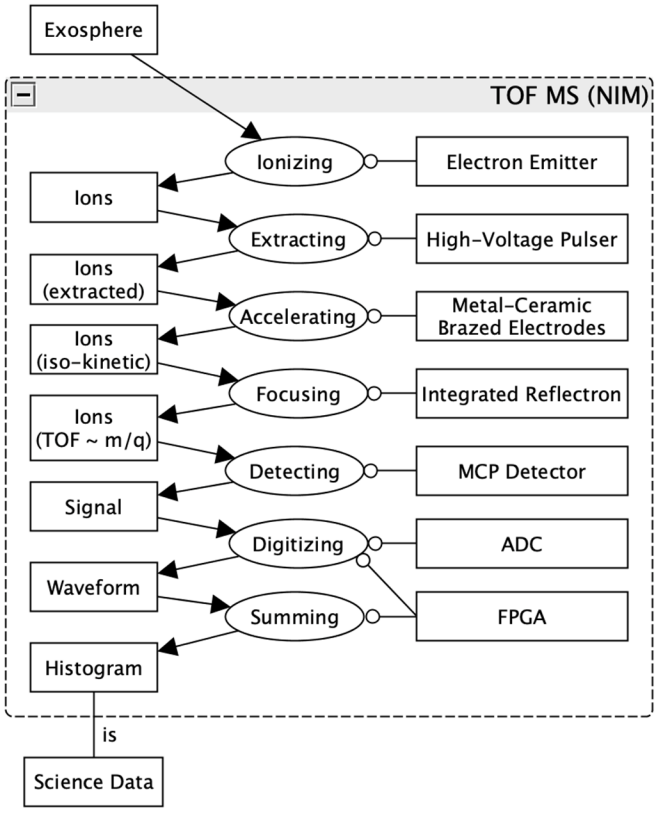

Figure 5 Architecture of NIM, as it was defined by the 'given' decisions at the outset of the project.

Having decided for a TOF architecture, an ion optics with a reflectron (an ion mirror), as opposed to a linear TOF design, was a natural choice considering the many advantages brought about by a reflectron (size reduction for the same flight path length and improved mass resolution). Solutions with a double mirror were briefly considered but soon dropped because incompatible with the allocated mass.

Electron impact was selected (G2) because it is well-established and easy to implement compared to other ionization mechanisms. It is also well-suited for the kind of atoms and molecules expected in the exospheres of Jupiter's icy moons: atomic species and simple inorganic molecules [11]. Besides, this ionization method is sufficiently versatile to accommodate for a capability to see the unexpected, such as more complex organic molecules that might be present in Europa's exosphere, or its purported water plumes.

An MCP detector (⌀ 10 mm) was baselined (G3) from the beginning. Alternatives, such as Channel Electron Multiplier (CEM), were excluded because of speed and size. An MCP can achieve ~500 ps pulse width, whereas a CEM typically generates 2–3 ns pulses. This difference translates in a factor ~2 in mass resolution (M/ΔM) in an instrument like NIM. Also, the reduced mass resolution impact negatively the signal to noise ratio (S/N), hence sensitivity, because in such a 'focusing instrument' M/ΔM ~ S/N. Moreover, a CEM is ~ 50% larger than an MCP for a significant mass penalty considering the need to enclose the detector in a ~10 mm Ta radiation shield. An MCP could provide maximum performance for less mass.

Metal-ceramic brazed elements and screen-printed electrodes (G4) were successfully qualified for previous missions (Rosetta, BepiColombo, Luna-Resurs). Moreover, the resulting 'monolithic' ion optics has several advantages compared to a 'discrete' metal-electrodes design. It is robust to mechanical and thermal loads, thus maintaining very precise electrodes positioning under stress, and it allows to build an 'integrated reflectron' as a seemingly continuous ion mirror [15] (Figure 6). Thanks to the narrow pitch of the spiral screen-printed electrodes, this design has a minimal field corrugation and optimizes the ratio between effective volume and size of the part. However, this technology has long procurement times for ceramic parts and requires complex manufacturing processes, such as brazing of ceramic and metallic electrodes that can withstand the launch loads. Moreover, the radiation hardness of the material used for printing the electrodes at the high total dose of JUICE was unknown (for details of radiation qualification with 18 MeV protons, up to 85 Mrad, see [16]).

Despite these complications, a two-decades-long experience with this technology led to commit early on to this heritage design (legacy decision). As discussed in Section 6 (decision D4), a failure during the PFM vibration test forced to revert this decision just a few months before PFM delivery, and revert to a discrete design to meet schedule. Ex-post, it is apparent that G4 could have been made differently for the ion source.

Figure 6 Integrated reflectors of previously built for Rosetta/RTOF and LUNA/NGMS (EMPA, Switzerland).

Decision About the Radiation Shielding (G5)

The need to shield the electronics and the detector differently emerged from the results of early simulation studies with GEANT4 [17]. On the one hand, maintaining the Total Ionization Dose (TID) of the electronics in the PEP Card Rack (Figure 1) below 50 krad required ~2 mm of Ta [18]. On the other hand, limiting the radiation-induced measurement (< ~10^5 events s^{-1} at the MCP at Europa, corresponding to ~10 counts s^{-1} in the spectrum factoring for the effective measurement time, Figure 3) required to enclose the ~10 cm^3 detector in a ~1kg 1–10–1mm Al-Ta-Al sandwich (details in [19], [20], [21], and [22]). These requirements made a clear case to minimize the volume of all elements to be shielded and to spot-shield the detector. Table 3 outlines the drivers and goals of this shielding strategy.

Table 3 Instrument radiation shielding strategy.

Design to (Driver)	Goal	Shielded element	Shielding element
End-of-life (Fluence, Si TID)	Survive <50 krad	Electronics	Vault (PEP)
Worst-case (Flux, cm^{-2} s^{-1})	Measure <10^3 s^{-1}	Detector	Local (NIM)

Decisions About the Electronics (G6-G7)

Given the significant mass required to shield with ~2 mm Ta the electronics, there was a big incentive to accommodating as much electronics as possible inside 'common vaults' to minimize the surface area to be shielded. PEP implemented this strategy by accommodating two sensors' electronics inside a Card Rack (CR), together with common primary DCCs and a DPU (both cold-redundant), providing power,

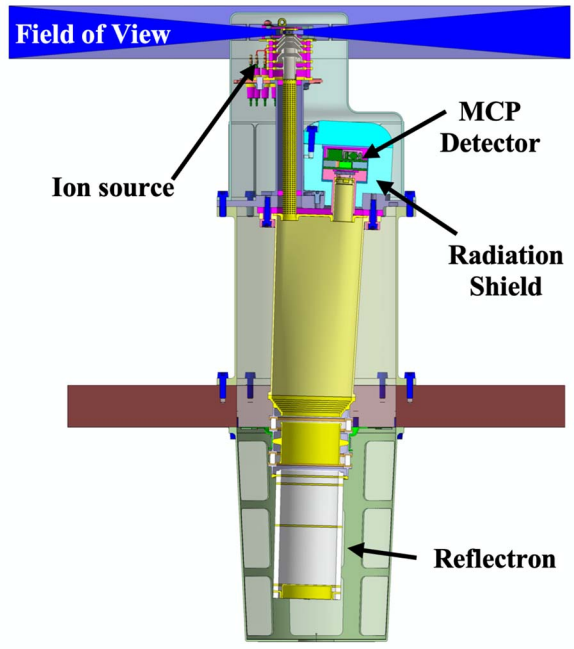

Figure 7 NIM mass analyzer's design as of early 2013. The blue areas show the field of view of the open ion source.

communication, and processing power to the four PEP-Lo sensors electrically interfaced to the spacecraft via the NU.

To minimize the amount of logic in NIM electronics and the associated board space, it was decided that the DPU process telecommands and telemetry, leaving the high-speed and time-critical control functions to the NIM electronics. This decision required the implementation of a 10 Mbps synchronous data interface between the DPU and NIM. It also required that the DPU be available to compress the raw data of NIM (and other PEP-Lo sensors) and transfer compressed data to the spacecraft's mass storage before the next measurement (measurement cadence: up to 1 s^{-1}).

The remaining functions to be provided by the NIM electronics that posed the most challenging requirements were the high-speed acquisition of the waveforms generated by the ADC (minimum 8 bits), their integration to produce histograms (without dead time), and the closed-loop control of the high-voltages of the ion optics. The selection of a 10 bit 2 GSPS ADC (ADC10D1000) as an optimal compromise between effective vertical resolution, power consumption, interfaces, and radiation hardness (100 krad) implied that:

- For a 2 GHz sampling rate, data are provided on four LVDS (Low Voltage Differential Signaling) lanes at 250MHz DDR (Double Data Rate, i.e., using both edges of the synchronous 250 MHz clock). Each of these data lanes is 10 bits wide, and data are spread over the lanes sample by sample so that the data processing unit requires data re-ordering.

- Given the parameters of the different operation modes, the maximum value accumulated in one bin of a histogram requires a 32-bit register.

The team concluded that no CPU-based solution was available in space-grade to meet these interface and memory requirements, together with the stringent timing requirement to provide closed-loop control of the high-voltages. Only FPGA and ASIC-based solutions were an option to fulfill the interfaces, memory, and timing requirements while being low power. Because the time and money to develop an ASIC were not available, an FPGA was baselined.

Early Design Concept

Figure 7 shows the design of the mass analyzer at this time, based on the outcome of these decisions and the first ion-optical simulations. The electronics began to take shape in the form of block diagrams and breadboards.

5. Architectural Decisions

The architectural decisions and trade-offs investigated in Phase B are listed in Table 4, ordered according to a well-known principle of mass spectrometry: 'follow the ions'.

A1. Ion Source

Ideally, NIM would use only an open-source (A1/Option 1), where the exospheric gas passes through a narrow slit and reaches the ionization region without touching any surface, thus allowing for the direct, uncompromised measurement of a pristine sample. However, this requires that the velocity vector of the inflow gas (i.e., of the spacecraft) be within the narrow Field of View (FoV) of such a slit, that is within ±5° about the nadir plane of the spacecraft. Very soon, however, this turned out to be incompatible with the evolution of the spacecraft attitude during flybys, which has to consider the attitude requirements of other instruments, too. This left two options: measure only in the very short time where the ram direction would be in this open source's FoV (~ 20 minutes around a flyby's closest approach) or implement a closed source in lieu of (A1/Option 2) or in addition (A1/Option 3) to the open-source.

Table 4 Key architectural decisions of NIM. The final decision is underlined.

Architectural Decision	Option 1	Option 2	Option 3
A1. Ion source	Open-	Closed-	Both
A2. Mechanism	Rotating (& 1 hole)	Shutter (& 2 holes)	–
A3. Emitter	Cold	Hot	–
A4. Detector	See Table 6		
A5. FPGA technology	Flash (RTG4)	Antifuse (RTAX)	SRAM (Virtex-4)
A6. PCB interconnect	External (backplane)	Internal (rigid)	Internal (flex)

A closed-source can be implemented with a so-called antechamber, a sphere placed on top of the instrument with one or more holes. This measurement concept is well-known and it has been successfully implemented in the past in space for Earth observation [23] and in interplanetary missions, including ONMS on Pioneer Venus [24] and NGIMS on MAVEN [25]. This solution allows measuring along the whole hyperbolic trajectory of a flyby because it provides a ~2π FoV about the axis of the hole(s) in the sphere. Besides, the sphere thermalizes exospheric neutrals and ions that are too energetic to be 'captured' by the open-source (i.e., > ~10 eV) thus extending the energy range of the instrument. Nonetheless, this sphere introduces the possibility of chemical modifications during the multiple impacts of the sample on its inner surfaces (e.g., fragmentation). This is undesirable as it may introduce artifacts in the mass spectra and complicate the reconstruction of the sample composition.

The preferred solution from a science perspective was to implement both an open and a closed source (A1/Option 3), the former used whenever the velocity vector is in its ±5° FoV, and the latter used in all other situations. This decision implied a substantial redesign of the mass analyzer, additional construction and operational complications, as well as a mechanism to switch between the two FoV (A2).

The changes to implement both sources, while feasible within the allocated mass and power, implied additional complexity in all domains: science (calibration of different modes), mechanics (implementation of mechanism), electronics (high-voltage design), FPGA and software (handling of multiple states and modes). Prioritizing science performance over technical and programmatic implications and risks, the team decided to implement both an open and closed source. This decision was not made based on a quantitative evaluation of the financial and schedule risk vs. science return but based on the perception that sufficient resources were available to accommodate this new scope, at the condition that the mechanism could be based on commercial motors modified and qualified in-house (see Section 6, D1).

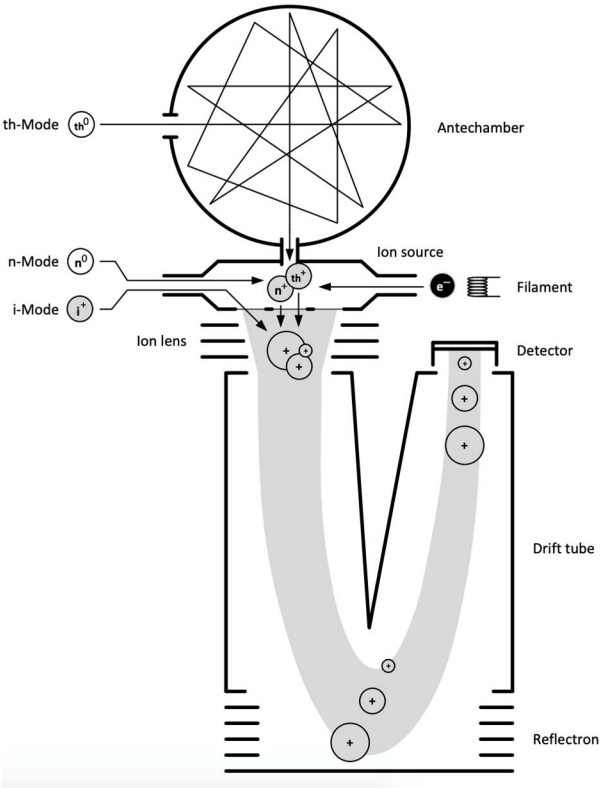

Figure 8 Sketch of NIM operational modes as results of taking decision A1/Option 3 (reproduced from [26]).

Figure 8 represents this decision and the instrument operational modes: 'thermal' (measurement of thermalized exospheric ions and neutral gas via the ante-chamber), and 'neutral' and 'ion' (measurement of exospheric/neutrals or ions via the open-source with/without electron emitters on). The viability of this architecture was simulated with SIMION and verified with the instrument prototype [26].

A2. Mechanism

The switching between the two FoV of the instrument (open and closed source as per A1) had to be realized within ~1s to avoid losing precious measurement time and spatial resolutions (spacecraft flyby velocity: ~4-7 km/s). Two designs were considered (A2): a rotating upper half of the sphere and a fixed sphere with a shutter (Figure 9).

The rotating sphere had a single hole at an angle of 30° from the axis of the mass analyzer (+Z) that, through rotation of the upper half of the sphere, could be oriented in the direction of the spacecraft's velocity vector. Moreover, by placing the sphere at a certain angle, the channel between the closed and open source could be blocked thus allowing to switch between the two FoV. The fixed sphere had two fixed holes at the same angle but towards the +Y and -Y axis, respectively, of the spacecraft's reference frame (to maintain the flexibility of flying the spacecraft in any of the two directions during a flyby).

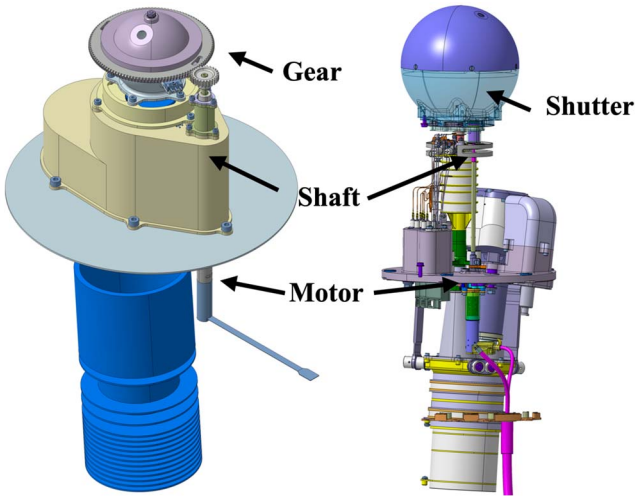

Figure 9 Left: rotating half-sphere design (A2/Option 1); right: fixed sphere with shutter design (A2/Option 2).

The switching between the open and the closed sphere was realized with a shutter closing and opening the small channel at the bottom of the sphere. The trade-off between the two was between performance and complexity: the rotating sphere ensured perfect alignment between the orientable hole and the spacecraft velocity vector, and a minimum ratio between the open and closed area, but it was more complex to implement. Initially, the rotating sphere was selected and a detailed design developed (Figure 9, left), but another requirement forced revert this decision and ultimately opt for the fixed sphere with shutter (Figure 9, right): cleanliness.

Indeed, it was realized that the rotating upper half of the chamber could not be effectively thermally coupled to the rest of the ion source and, therefore, it could not be decontaminated in flight, before each flyby, using the ceramic decontamination heater inside the ion-source. Accordingly, the upper half of the chamber would act as a cold-trap, potentially cumulating contamination during ground operations and in-flight in a critical location of the instrument (i.e., the sample introduction system). On the other hand, the fixed sphere could be heated efficiently, together with the rest of the ion source, at >80 °C, using the 5 W screen-printed ceramic heater in the ion source (details about heater's material and radiation qualification in [16]).

A3. Emitters

The ionization of neutrals via electron impact is typically performed using electors of ~70 eV generated by a cathode, for a current from ~0.1 to ~1 mA. Both 'hot' and 'cold' cathodes exist. The former consists of thermionic emitters, and the latter of a variety of technologies based on field-emission: Spindt cathodes (Sri International Inc., see [27] and [28]), Field Emitters Arrays (e.g., all-metal FEA from the Paul Scherrer Institute, Villigen, Switzerland, [29]) and carbon nanotubes [30]. Cold cathodes require as little as ~100 mW to operate, whereas hot cathodes require at least ~1 W; hence, there is a clear advantage in using cold cathodes on a power-constrained instrument like NIM.

Both hot and cold cathode emitters have spaceflight heritage. Hot cathodes were implemented in RTOF [3] on Rosetta, which included W(Re 3%) wires mounted on a spring-loaded socket. This design had the advantage of spreading emission along the length of the wire, thus allowing for higher emission current before hitting the limits imposed by space-charge effects. Cold cathodes were implemented on the Neutral Gas Experiment onboard the Vega spacecraft to the Halley comet in 1986 ([31] and [32]) and in the COPS ram ion source of Rosina [3] on Rosetta.

Despite the advantages of cold cathodes, the team ruled out this solution after consulting with experts in the field and realizing that there were no off-the-shelf solutions that could be implemented without a significant effort to demonstrate their suitability and reliability for the mission. In particular, at the required current level, there were unresolved reliability concerns of these technologies related to oxidation and adsorption on the emitter surface, which would be difficult to address. As far as carbon nanotubes were concerned, there were also emission current stability concerns. Finally, lack of evidence that these technologies could operate and survive in the harsh Jovian radiation environment made them TRL ~3.

Table 5 Trade-off between thermionic emitters.

Property	Y_2O_3 (baseline)	BaO (backup)
Lifetime (cycles)	*>10'000*	1'000
Power (W at 300 μA)	1.2	*0.85*
Emission at 1 W (μA)	> 50	*600*
Conditioning	*Simple*	Complicated
Heating current (A)	*0.9*	1.15
Venting to air	*No issue*	Cathode poisoning

Eventually, thermionic emitters based on enhanced-lifetime Y_2O_3 and BaO coated discs (Kimball Physics Inc., USA) were chosen as baseline and backup solution (Table 5), respectively. Notwithstanding the higher power consumption (~1.5 W after all losses are accounted for), thermionic emitters were very mature off-the-shelf components with space heritage (e.g., BaO was implemented in STROFIO for BepiColombo) and were expected to be robust to radiation effects. Thus, they carried a much lower risk. Moreover, long lifetime tests were necessary to prove that the filament could survive the ~10,000 h of operation for the entire mission, thus calling for a quick convergence on a technology to build and start these tests as early as possible. At the time of writing, seven filaments of each kind have been run at a nominal emission current of 300 μA for ~2,000 h of operation, including periodic on-off cycling every 8 h, showing nominal performance. Cold cathodes remain an attractive option for future missions, but a dedicated program is needed to increase their TRL beyond 3–4.

A4. Detector

As a key element for the performance of the instrument, the MCP detector was subject to plenty of attention in Phase B. There was an impelling need to finalize its baseline and build a flight-like detector to verify experimentally its capability to measure at Jupiter (with Europa instantaneous flux as sizing case). The four decisions to be made about the detector are summarized in Table 6.

Table 6 Detector decisions; the second option is generally preferable but harder to implement than the first one.

Decision	Option 1	Option 2
I. Anode	<u>Single</u>	Double
II. Floating	No	<u>Yes</u>
III. Signal read-out	<u>Single ended</u>	Double ended
IV. Anode	Disc	<u>Spiral</u>

I. Whether the detector should have a single or a double anode. The latter has the advantage of allowing for two signal lines with different gains to be implemented [33], for higher dynamic range, redundancy, but also increased complexity of implementation (more signals to be routed through the shielding, extra space required in the electronics).

II. Whether the detector should be floating or not. The former gives the advantage of more degrees of freedom in the ion-optics design and detector operation because the final potential of the ions is not constrained by the ~2 kV of the front-plate of the MCP detector assembly, but it requires to implement ~nF capacitors on the signal path next to the anode. Such capacitors have poor high-frequency performance and are voluminous, thus working against the goal of minimizing the detector's size to minimize the shielding mass.

III. Whether a single (50 Ω) or double (100 Ω) ended signal read-out should be implemented. The latter gives the advantage of more signal (due to the lack of the termination resistors to ground), more freedom of selecting the anode impedance due to the presence of a transformer, and a better common-mode noise susceptibility if well-balanced. However, this has the disadvantage of requiring more custom (most standard parts with good high-frequency performance are tuned for 50 Ω). Moreover, feeding the detector signal directly to the ADC input (which is also differential) did not seem feasible with sufficient performance. This also required the implementation front-end gain stage, which meant a conversion to single-ended somewhere along the signal path or a differential gain stage, such as a balun, which did not exist with sufficient bandwidth (from ~DC to ~1 GHz).

IV. Whether a disc or spiral anode should be implemented. The former provides larger signals, but not a perfect impedance matching, whereas the latter provides a better matching, but a somewhat lower signal due to the impedance termination at one side of the spiral.

Different anodes designs were conceived (Figure 10) and the expected pulse width was calculated for different types of PCBs with ε_r ranging from 2.9 to 10.2 using PCB Toolkit (v6.64, Saturn PCB Design, Inc.).

Figure 10 Different type of MCP detector anodes: circle, broad spiral, narrow spiral, and double spirals (last two). In all cases, outer anode ⌀ = 8 mm, red circle gives the active MCP area.

The resulting pulse width was ~170–270 ps and 480–780 ps for anodes with 2 and 7 spiral turns, respectively, with the lower values of the range for $\varepsilon_r = 2.9$ and the higher values for $\varepsilon_r = 10.2$. Note that pulse widths below 500 ps are well-matched with the 2 GSPS acquisition rate of the ADC. A selection of these designs was realized and tested in a prototype detector setup.

We decided to implement a single anode design (Decision I) because the double anode design required a more complex solution for the data acquisition using more power, and more PCB space than were available for this design. Alternative electronic designs, using newly available parts that had not space heritage yet, would have met the power and PCB space requirements, but presented a significant development risk and thus were rejected.

Given the test results, a single-spiral anode with 4 turns and 0.9 mm width was selected (Decision IV, similar to the second design in Figure 10) as an optimal compromise between pulse width (290–470 ps) and impedance matching.

While we managed to overcome most of the problems of a double-ended detector and build a working laboratory prototype, the performance was not good enough to justify the effort to implement this design in flight-quality, also considering that significant uncertainty remained about its feasibility. So single-ended was selected (Decision III).

The results of ion optics simulations made a strong case for selecting a floating detector (Decision II), despite the disadvantages due to the bulky high-voltage capacitors. To minimize the volume of the detector, a compact design based on a folded rigid-flex PCB was devised. The resulting detector has a volume of only 8 cm^3 (Figure 11). This design, enclosed in a 1–10–1 mm Al–Ta–Al radiation shield weighing 1.1 kg, was verified by simulation and experiments with 11–345 MeV (details in [19], [20], [21], and [22]).

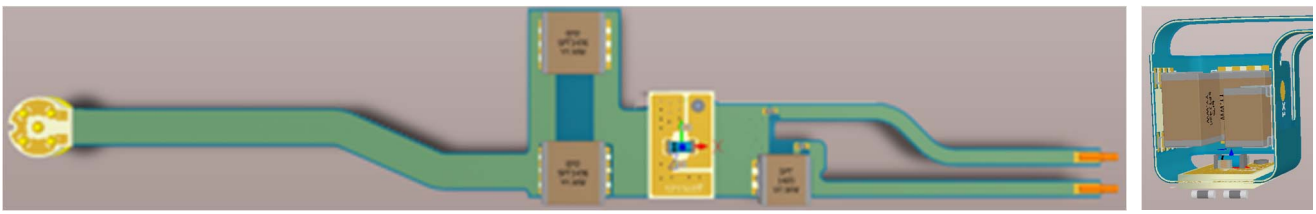

Figure 11 Left, flat rigid-flex PCB (120 x 35 mm); right, folded detector (20 x 23 x 23 mm).

A5. FGPA

The most critical architectural decision about the electronics design was the selection of the FPGA, because of the impact on the electronics design, mass and power, and programmatic aspects. Indeed, a different choice of FGPA leads to different auxiliary components needed for its implementation (programming), workflows (depending on whether or not it is reprogrammable), power consumption (a very scarce resource!) and ultimately impact on cost and schedule. At the time of making this decision, in early 2017 (PDR), a new component was being launched on the market, Microsemi's RTG4: a radiation-hardened by design and low-power FPGA. This component would have perfectly fit the requirements of NIM and was indeed chosen as the initial baseline (Figure 12, top). However, this brand new FPGA was considered by ESA to be not enough mature for JUICE; therefore, the team had to devise alternative solutions using components that were already available and deemed acceptable for flight.

Two alternatives were identified, based on reprogrammable (Xilinx's Virtex-4) and non-reprogrammable (Microsemi's RTAX-4000) chips. The latter required a multi-chip architecture requiring as many as four FPGAs because of the limited memory resources of the RTAX-4000. Specifically, 192 kB of BRAM is needed to store a complete histogram compared to 67.5 kB available in one chip. Solutions to use external fast SRAM were prohibitively expensive in terms of power consumption (~2–3W) because the address and data ports of the external chip has to be running during the whole acquisition time, whereas for internal memory only the ports of one BRAM per data lane are active at any given time.

A design based on the reprogrammable Virtex-4 would be identical to the RTG4 baseline design except for the MRAM needed to hold the FPGA configuration image and a small FPGA or microcontroller needed to load the FPGA's SRAM based configuration memory at power-up. In principle, even a simpler solution to configure the FPGA using an external PROM (using the so-called master-serial mode) exists, but the only identified space-grade parts to do so (XQR17V16 from Xilinx and 3DPO64M08VS2299 from 3D PLUS) were rated only at 50 krad TID, thus not meeting the ≥100 krad requirement for the electronics in the PEP electronics' vault (CR designed for 50 krad, leading to 100 krad with a margin of 2). Table 7 summarized the key findings of the detailed trade-off study that led to selecting Virtex-4 as baseline (A5/Option 3).

Although this solution provided the benefit of the flexibility of a reprogrammable FPGA, which can be updated even after launch, it introduced significant design complexity. First, Virtex-4 does not have any native Triple Module Redundant (TMR) flip-flops. Therefore, three standard flip-flops had to be combined, which could be done to some extent by the synthesis tool, but also at the level of the functional blocks. This also posed a risk, because an improper implementation of TMR could result in a logic yet more susceptible to SEUs. Moreover, a TMR design created from standard flip-flops is vulnerable, in that the necessary interconnects between the flip-flops are controlled by an SEU-susceptible configuration memory. Therefore, it was mandatory to implement a scrubbing mechanism that periodically refreshes the FPGA configuration (from a calculation of expected error rate, scrubbing rate should be once every 1–5 minutes). Finally, TMR at minimum triples (or more, depending on the actual design) the required logic resources, and a higher level of utilization may lead to a yet higher power consumption.

All in all, the choice of the FPGA design of NIM is far from the ideal technical solution that could have been implemented with state-of-the-art technology, but it was considered the best solution within the constraints of the project.

The final design baseline includes a Microsemi's RTSX72 non-reprogrammable FPGA plus an MRAM to configure and scrub the Virtex-4. The system also has the flexibility of configuring the Virtex-4 via the common DPU, which takes much longer but is a convenient fallback solution.

A6. PCB interconnect

The size of the electronics vault was estimated based on the PCB area of previous similar instruments built by the team, resulting in the allocation of two 125 x 130 x 58 mm frames. Early design concepts of the electronics spanned across several boards, including a mixed-signal board, as follows:

i. *Controller PCB*, a half-frame board accommodating FPGA, ADC, the detector front-end, and the mechanism motor controller.

ii. *Pulser PCB*, a half-frame board hosting the high voltage pulser circuit.

iii. *Low-voltages PCB*, a half-frame board accommodating the low-voltages power supply for the ion source's electrodes and the controller of the electron emitters.

iv. *High-voltages PCB*, a half-frame board including all high-voltage power supplies for the electrode of the ion source, the reflectron, and the detector.

v. *Programmer PCB*, a small satellite board attached to the controller holding the components necessary to program the Virtex-4.

Boards ii, iii, and iv had to be connected to board i, where the instrument control logic relies. How these PCBs would be connected was critical because it had widespread effects on the design of the NIM electronics, of the NU CR in general, and ultimately on the mass of the instrument.

Table 7 Decision matrix for the selection of the FPGA; + means better, - means worse.

Criterion	RT4G150		RTAX4000SL		XQR4VFX60 (Virtex-4)	
Power cons.	++	2.88 W	-	4.05 W	-	3.96 W
Extra mass	++	0 g	- -	+470 g	- +	~45 g (with MRAM) 0g (with PROM)
Design process	++	Flexible	- -	One shot	+ -	Flexible (with MRAM) Less flexible (with PROM)
Radiation hard	+	By design	+	By design	-	By screening
TMR	+	FF & SET filters	+	FF	- -	To be implemented
Configuration	+	Flash memory	++	Anti-fuse	- -	SRAM (need scrubbing)
Flight heritage	-	None	++	Extensive	+	Some
Assembly process on PCB	-	None approved (CG1657)	++	Well known (CQ352)	+	Project qualification (CN1144)
Cost estimate	+	~$250,000	- -	~$1,100,000	++	~$100,000
Availability	-	New component	+	Available immediately	+	Available immediately
Risks	Results of EV / QML-V qualification tests. Potential PCB assembly issues.		Difficult design process. High cost.		Development efforts to implement TMR and scrubbing.	
Non-compliances	None.		Exceed mass and power allocation, do not meet all science requirements.		Exceed mass and power allocation.	

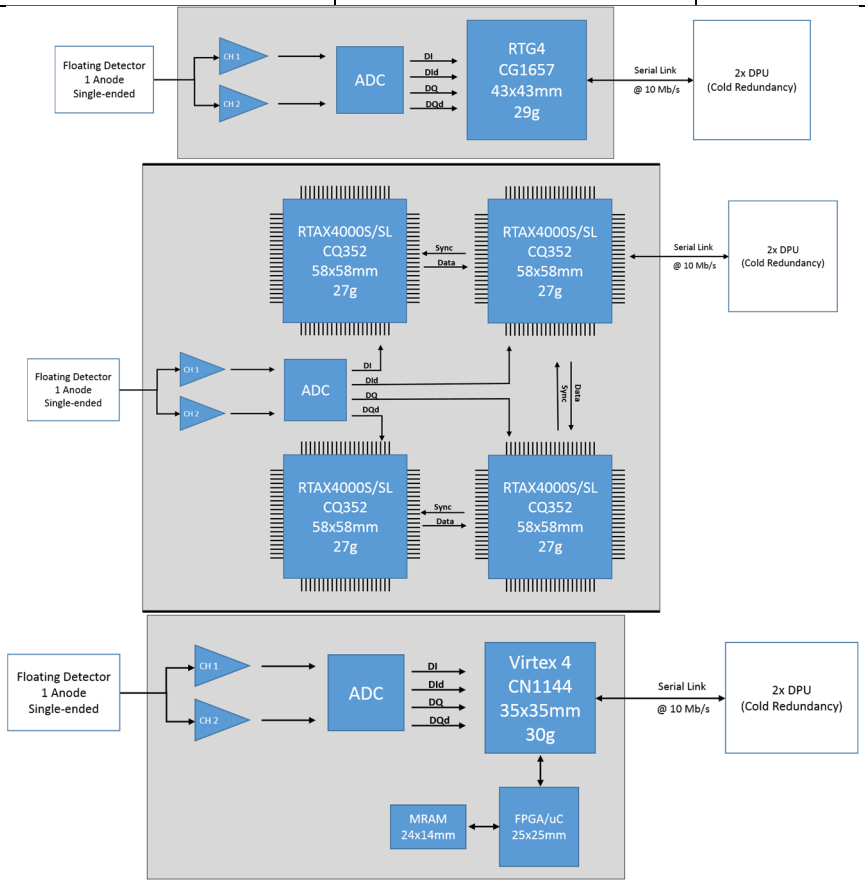

Figure 12 The different designs of the front-end and high-speed data acquisition via FPGA considered for NIM in Phase B (2016) based on RTG4 (top), RTAX4000 (middle), and Virtex-4 (bottom). A nearly identical diagram can be drawn for the bottom solution with a 16x17 mm PROM instead of an FPGA or a microcontroller together with MRAM.

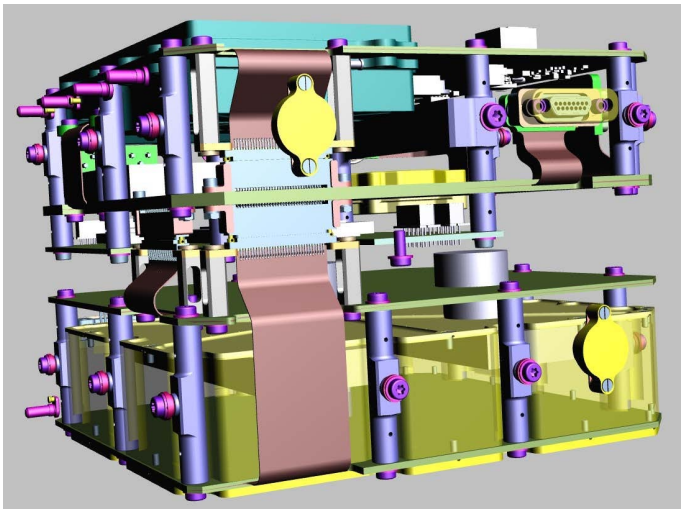

Figure 13 Rendering of the interconnection among boards by means of rigid-flex PCBs (A6 / Option 3).

The trade-off for the PCB interconnect was the following:

- An interconnect external backplane (A6/Option 1) was preferable for the electronics design, as it maximized the board area available for the placement of components. However, it created a dependency with the mechanical design due to the time needed to finalize the definition of the connectors. Moreover, closing the opening in the 2 mm Ta-thick electronics vault, the CR, to avoid creeping-in radiation is all but a trivial task, hence increasing the complication and risks associated with the CR mechanical design.

- An interconnect with internal rigid connectors (A6/Option 2) was preferable for manufacturability, as it allows to rely on standard rigid PCBs. However, rigid connectors require plenty of board area that cannot be used for placing components, thus increasing the risk that the allocated board space be insufficient. Because of the heavy mass penalty associated with an increase in the dimension of the CR (either with an extra frame or with larger frames) this solution had a high-risk of forcing later to descope functionality to fit in the defined frame size, or to exceed the mass allocation.

- An interconnect with internal flex connectors (A6/Option 3) would overcome the limitations of the other two solutions, and completely decouple the problem of the internal connection of electronics with the mechanical design of the CR frames, but at the cost of the high complexity and risk of manufacturing many-layers rigid-flex PCBs.

Eventually, Option 3 was baselined (Figure 13) on grounds of its apparent benefits, and somewhat not fully aware of the manufacturing risk that this solution was embedding. Indeed, the controller PCB ended up being an 18-layer design, whose manufacturing was considered to be of the highest risk by the supplier. Mitigating this risk required a layout rework (~1 month of schedule delay) and the acceptance of the possibility that the manufacturing of the board might fail. Although everything resolved for the best in the end, ex-post it would have been appropriate to consider the PCB manufacturing risks in more depth during the performance of this decision's trade-off.

6. Design Decisions

There is always some degree of ambiguity about what is to be considered an architectural or a design decision. An instrument like NIM is the outcome of hundreds of decisions, and there is a fuzzy boundary between a handful architectural decisions that ought to be taken early on and cannot be postponed (barring the perdition of working in a vast solution space), and the rest of design decisions that can be defined as part of 'normal work', as we idiomatically said of the application of engineering skills to solve a well-defined challenge.

While it is easy to call a very local choice that has no impact on the rest of the system a design decision (e.g., choosing a particular electronic component for a memory, or a specific conductive coating of a non-metallic parts) there are several decisions at the 'mesoscale' whereby drawing a line is not trivial. While criteria exist to qualify a decision as architectural [13], the boundary between architectural and design decisions remains fuzzy and somewhat dependent on the particular perspective that one takes on a system. For limitation of space, we focus hereafter on a selection of design decisions. In the end, we provide an overview of the design that synthesizes other decisions that we cannot discuss here.

D1. Motor Magnet

To operate the shutter mechanism, a modified commercial motor was baselined. Two alternatives were considered: brushless DC servomotors series 0824 (⌀ 8 mm x length 24.1 mm, mass: 5.2 g, NdFeB magnet) and 1628 (⌀ 16 mm x length 28 mm, mass: 30 g, SmCo magnet) by Faulhaber Minimotor SA, Switzerland. The former was better because of the smaller size and lower mass, whereas the latter was better because of the higher radiation hardness of SmCo compared to NdFeB [34]. While a ⌀ 8 mm motor with SmCo magnet was feasible, a standard magnet of that size was not available and a new dimensioning of the coil was required, for a lengthy and expensive custom design.

Table 8 A selection of design decisions about NIM.

Design Decision	Option 1	Option 2
D1. Motor magnet	SmCo	NdFeB
D2. Emission controller	DC	AC
D3. High voltage pulser	1 switch	2 switches
D4. Ion source electrodes	Nb+Ti/Mo	MoCu
D5. Automated optimizer	Yes	No

To make a decision, radiation tests were performed to verify the degradation of the two magnets at the dose level of the mission. Both commercial motor's NdFeB and SmCo magnets were irradiated with 18 MeV p^+, at the same cyclotron facility described in [16], up to a target dose of 15 Mrad (mission dose behind ~2 mm Al x margin of 4), with a 50 nA beam current for 45'. The magnets were mounted on a rotating mechanism allowing to uniformly expose it to the beam inside the irradiation chamber in vacuum. An additional irradiation with the static magnet and a Pt-1000 temperature sensor bonded on its surface was performed to exclude thermal effects. The magnetization was measured before and after irradiation with a Gauss-meter and a custom adapter ensure reproducibility of the probe positioning.

The irradiation on the rotating magnets causes a loss of magnetization of ~16% for NdFeB and ~2% for SmCo (the latter considered to be within the measurement error). The temperature of both (static) magnets during irradiation never exceeded 80 °C, thus excluding that losses of magnetization could be due to exceeding the Curie temperature at bulk level (~300 °C for NdFeB and ~700 °C for SmCo). However, this could not exclude damages due to local thermal effects.

To understand the nature of the observed damages, ~5 months after irradiation, when the magnets were not radioactive anymore, samples of the irradiated magnets were sent to the motor provider for characterization and re-magnetization. The NdFeB sample showed magnetic moment losses not exceeding 10%, which could be explained in terms of annealing effects, or differences in the measurement setup (manual measurement at the irradiation facility with handheld magnetometer compared to a better measurement with Helmholtz coil). After re-magnetization, the NdFeB magnets recovered the original magnetic moment entirely. The SmCo sample was within ±1% the magnetic moment before irradiation, indicating that it did not experience any radiation damage or that annealing occurred. These results demonstrated that the radiation did not induce significant irreversible structural changes in the magnets, and probably only caused local demagnetization, due to exceeding the Curie temperature, that could be fully recovered with a re-magnetization. These thermal effects could be considered an artifact of the accelerated dose rate of ground tests compared to space, thus granting that the performed test be indicative of a worst-case scenario that will hardly be approached in reality. In any case, even considering the worst-case loss of the magnetic moment of the NdFeB sample (~16%), the residual magnetic moment was yet higher than that of a SmCo (weaker) magnet of the same size (~30% lower than for a same-size NdFeB magnet). Therefore, the off-the-shelf NdFeB commercial motor was baselined, with minor modifications performed in house to make it suitable for flight (Parylene coating of the magnet, use of dry MoS_2 lubricant, and replacement of plastic parts).

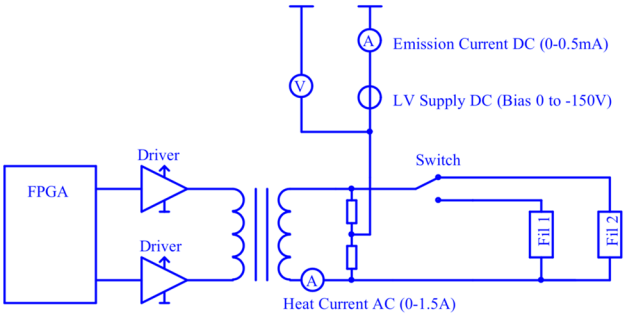

Figure 14 Simplified schematics of the AC filament controller, showing the two cold-redundant filaments.

D2. Emission controller

Two different types of emission controllers were considered, using DC or AC to power the thermionic emitters, both of which had a heritage of implementation in space-grade (TRL 8). An engineering model of the AC filament controller (heritage design from [6]) showed an efficiency ~10% higher for the same type of ~1 W thermionic filament than a previous DC controller after considering all DC/DC converters efficiency. Therefore, an AC controller was selected and implemented (Figure 14), despite the disadvantage of having a ~30 kHz frequency that could be an EMC concern, and the less reliable housekeeping value of heating and emission current.

D3. High-Voltage Pulser

The performance of a TOF MS is highly sensitive to the shape of the high-voltage pulse applied to extract the ions in the acceleration region of the ion source. Ideally, a perfect rectangular pulse with a height of ~500–800 V and a duration of a few hundred ns is required. In practice, the performance of switches (MOSFETs) available in space-grade, derating requirements, and high-frequency effects (e.g., Gibbs phenomenon at sharp pulse edges) only allow to approximate this ideal behavior. For NIM, the 100 krad radiation hardness requirement limited the choice of high-voltage MOSFETs to a handful of candidates: Fuji's 2SK4189 and 2SK4190, and International Rectifier's IRHNJ67434 and IRHNJ67C30. The latter was baselined because of the better voltage rating and lower capacitance compared to the other components.

Yet, the desire of a ~500–800V pulse height led to a trade-off between two designs: using one or two MOSFETs in cascade (Figure 15). The former is limited by the 80% derating requirement to 480V but faster, ~5–6 ns fall time, whereas the latter allows to cover the full range of voltage after

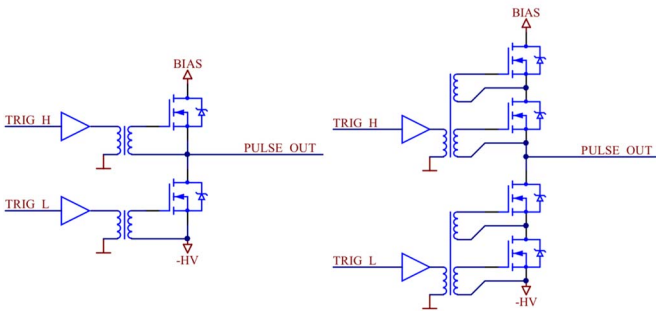

Figure 15 Simplified schematics of the 'fast' (left) and the 'slow' (right) pulser.

derating but is slower (+2–3 ns). Measurements with engineering models and the instrument's prototype (Figure 16) showed that the two-switches ('slow') design led to low mass resolution for low masses (<100 u) and a loss of sensitivity for pulse heights > ~400 V, thus failing to deliver the main utility of this design. This led to opt for the one-switch ('fast') design despite the pulse amplitude limitations due to derating. The dependence of the mass resolution on mass, proportional to √m, indicates that the pulser switching speed is a limiting factor of the instrument's performance.

D4. Ion Source Electrodes

Ion sources previously developed by the same team were manufactured as two-pieces electrodes with Ti_6Al_4V (NGMS/Luna-Resurs) or Mo (RTOF/Rosetta) conical electrodes welded to Nb rings, which were brazed on ceramic insulator (Al_2O_3 97.6%). The manufacturing of one-piece electrodes made of Nb was hard, and the Nb surface finish was insufficient for ion-optical applications. On the other hand, Ti_6Al_4V and Mo could not be directly brazed to the ceramic insulators because of the CTE mismatch. Therefore, Nb rings or Ti_6Al_4V plus copper rings had to be used in connection with the ceramic insulator, for a complicated (yet proven) manufacturing process.

During the design of NIM, we identified a new material that could allow for a single-piece electrode design, easy to manufacture, and with the same CTE of alumina: Mo85Cu15, a sintered alloy. By using this material the number of parts and joining processes could be reduced. The trade-off was choosing between a high-TRL and low-TRL solution in consideration of the reduced manufacturing complication.

Extensive characterizations of the new material and processes were performed, including mechanical tests [35]. Based on this positive evidence, the new material was baselined for all ion source electrodes except the last one, maintained in Ti_6Al_4V because it was connected to a drift tube made with the same material (Figure 17).

Nevertheless, the ion source failed unexpectedly during the PFM sensor vibration test in November 2019, with a clear cut

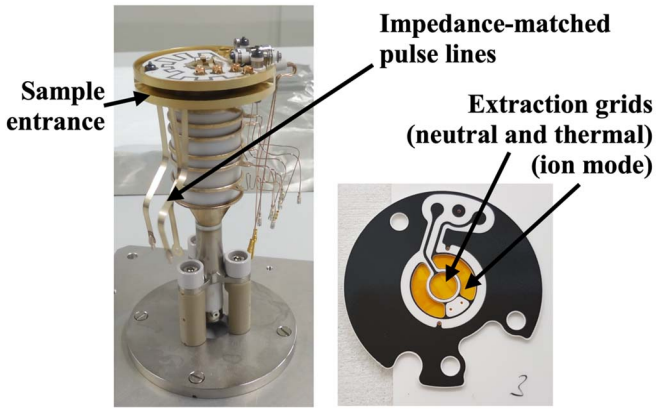

Figure 17 Ion source stack (left) and metallized ceramic extraction electrode (right).

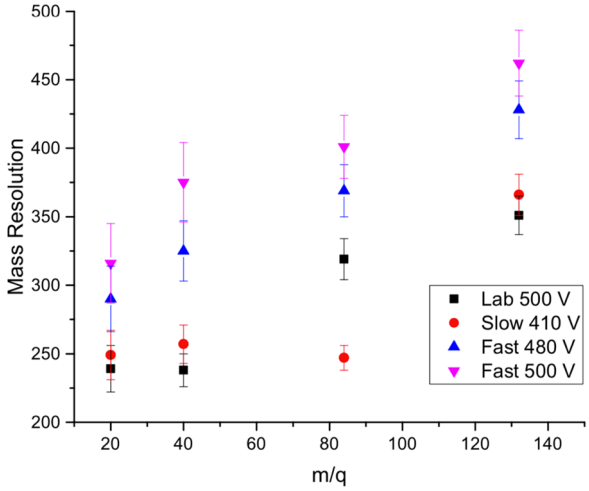

Figure 16 Variation of the mass resolution for the two pulser designs at different pulse heights.

breaking point at the joining between the last electrode and the drift tube (i.e., the only electrode made in the 'old' material Ti_6Al_4V). Ex-post, the most likely cause for this failure was traced to the plating process applied before brazing. All electrodes were plated with TiAlN followed by W and Cr + Au. This process proved to be suitable for the new Mo85Cu15 material, but for reasons that are yet to be understood did not provide a proper surface finish for the old Ti_6Al_4V material, which should have been instead Ni plated, as in the past. This process change lowered the TRL of the part, compromising the structural properties not of the new material, but of the old material treated with a new process.

As the ion source was not mechanically tested at subsystem-level, but only at system-level, the issue was discovered very late in the project, just four months before the deadline to deliver the PFM sensor for integration in the PEP NU. Because the lead time to procure new monolithic ion sources was ~6 months, the monolithic design was abandoned in favor of a new design based on discrete metal-electrodes (Figure 18) that could be built in-house. From an ion optics point of view, the discrete design is already proven as it the same as the instrument prototype [26]. From the mechanical point of view, this is very simple, and an early finite-elements

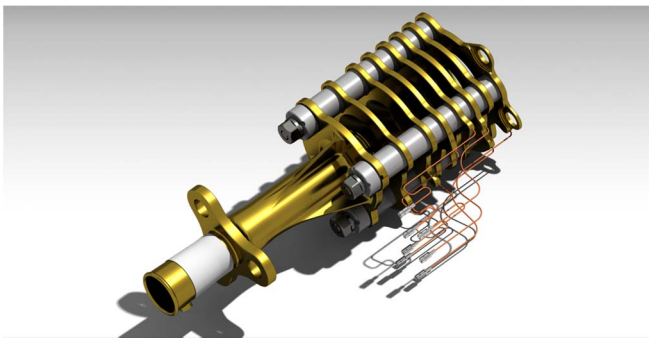

Figure 18 The redesigned ion source using discrete metal electrodes made of gold-plated aluminum (7075), standard ceramic insulators (Al_2O_3 and ATZ) with titanium bolts spot welded to the first titanium lens, and titanium nuts.

model indicated that the first modes could be expected above 300 Hz, thus meeting the requirements. This new ion source is in manufacturing at the time of writing and will be available for integration in the PFM in February 2020.

The lessons learned are two. On the positive side, the Mo85Cu15 remains a possible solution for the realization of robust monolithic ceramic-metal brazed ion sources with a simpler manufacturing process, as the structural failure could not be attributed to the new material, but rather to an incorrect process applied to an electrode made with the old material. On the negative side, it shows, ex-post, that the adoption of a complicated monolithic ceramic-metal brazed ion source (the 'given' decision G4) may have been an unnecessary complication from the beginning for this instrument. Ex-ante, building the 4th instrument in a row using a heritage technology that worked seamlessly for the previous two decades appeared as a natural choice, even if a simpler discrete design might as well have met the requirements. With today's awareness of the risks, a thorough trade-off study, qualification program, and change control will have to be performed for metal-ceramic brazed elements in future instruments.

D5. Automated Optimizer

An automated particle-swarm optimizer turned out to be very effective to find optimal settings of the ion optics of TOF mass spectrometers [36]. This algorithm allows for a broad exploration of the parameter space of an ion optical system in search of an optimal set that maximizes a score function (e.g., amplitude, peak width, or a combination thereof). During this exploration, it can happen that the settings of the ion optics be far away from nominal-operation ones. In this case, the electrons emitted by the filament (~100s μA) may end up on any electrodes of the ion optics and charge it, if such an electrode has not the capability to sink current. When an electrode charges up, the functionality of the optimizer is impaired, because the relationship between the applied potential and the effective potential of that electrode in the next step(s) of the optimization becomes arbitrary. Either the instrument can detect charging, stop the optimizer and power supplies, and wait for discharging before continuing the optimization, or the power supplies of the ion optics shall be designed with the capability to sink the emission current.

On an instrument like NIM, highly constrained in terms of power and board space, there is an incentive to design simple circuitry, such as one-quadrant power supplies. Under nominal settings of the ion optics, the current flowing through the electrodes is substantially null; therefore, a one-quadrant power supply suffices. RTOF [3] on Rosetta, for instance, was designed this way. Unfortunately, this design is incompatible with a particle-swarm optimizer for the reasons related to charging described above. However, implementing a two- or four-quadrants power supply (depending on polarity requirements) approximately doubles the development effort and complexity of the circuitry, thus requiring more board space.

Experience with previous instruments showed improvements in mass resolution and S/N up to factor ~2 by using an automated particle-swarm optimizer instead of a manual optimization of the ion optics. Moreover, manual optimization would be complicated to handle for NIM, because of the long signal travel time between Earth and Jupiter.

The eventual decision for NIM was to implement power supplies with a capability to both source and sink currents to support the optimizer. The emission current during optimization, however, is limited to <150 μA, instead of the nominal ~300 μA, to facilitate the design of converters that could both support optimization and have a very low standby power during nominal operation of the ion optics.

Overview of the Final Design

The final design of the sensor (with the new discrete ion source) and of the electronics are shown in Figure 19 and Figure 20. These representations summarize the outcome of all the decisions discussed here, plus a few more that could not be discussed here for limitations of space.

For example, the structural supporting structure in Figure 19 is different from Figure 7's, which was conceived for the original concept of the NU including an AlBeMet baseplate to which the sensors were bolted onto. This baseplate was

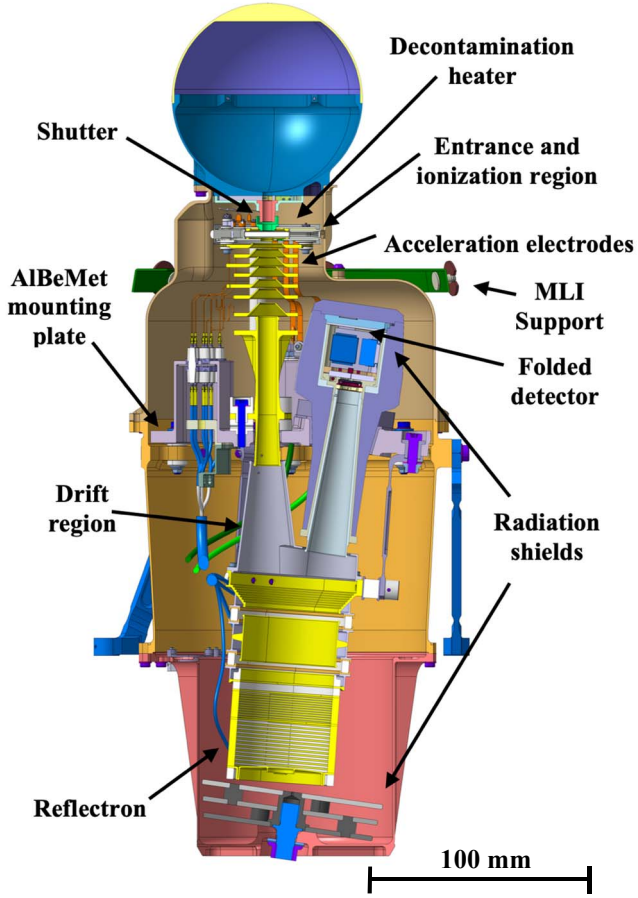

Figure 19 Section of the NIM sensor's flight design.

later replaced by a carbon fiber panel for higher handling safety, requiring a structural redesign of the sensor with an internal AlBeMet mounting plate supported by isostatic feet to compensate for the structural stress due to panel deformation. Above this AlBeMet plate, the only allowed materials are metal and ceramic to maximize cleanliness.

The final implementation of the shielding deviates from that tested in [22] in that the heavy-Z material of the graded shield has been changed from Ta to W85Cu15 for better manufacturability. In addition, the 6 mm Ta disc at the bottom has been split in three 2 mm discs, distance by 4 mm, to take advantage of the increase geometrical deviation of the electrons away from narrow open channel toward the MCP, as suggested by limited experimental results (unpublished) during the detector radiation testing campaign [22].

It is worth noting that the thermal control of the NIM sensor is entirely passive. The unit does not need any survival or operational heater. The whole sensor head is enclosed by Multi-Layer Insulation (MLI) up to the MLI support shown in Figure 19. The part of the sensor above the panel faces the space environment, whereas the part below the panel faces a –50 °C spacecraft cavity. The 5 W heater in the ion source is only operated several hours before a measurement to clean the ion source and the antechamber at > 80 °C.

7. RESULTS

The first mass spectrum measured with the PFM is shown in Figure 21. It has been acquired with the instrument in the configuration of Figure 22. The voltages were optimized by hand starting from the simulation results of the thermal mode.

The measured mass resolution of ^{84}Kr for the residual gas measurement is 305 ± 15 and the S/N 608. Additional measurements were performed with a 2.7 km/s neutral gas beam consisting of hydrogen and krypton in CASYMIR [37]. The mass resolution of ^{84}Kr in thermal mode was 404 ± 25 and the S/N 235. The mass resolution of ^{84}Kr in neutral mode was 417 ± 27 and the S/N 1,456. At the current state, the instrument performance is the same as the prototype [26]. When the sensor will be integrated with the flight electronics, supposed to be better than laboratory electronics, using short cables, mass resolution and S/N are expected to improve.

The replacement of the monolithic ion source with the discrete ion source (see Section 6, Decision D4) is not expected to have a significant effect on performance. Indeed, the prototype, ion-optically identical to the PFM, was realized with a discrete ion source and had the same performance as the PFM with the monolithic ion source. Nevertheless, the calibration of the sensor will have to be repeated.

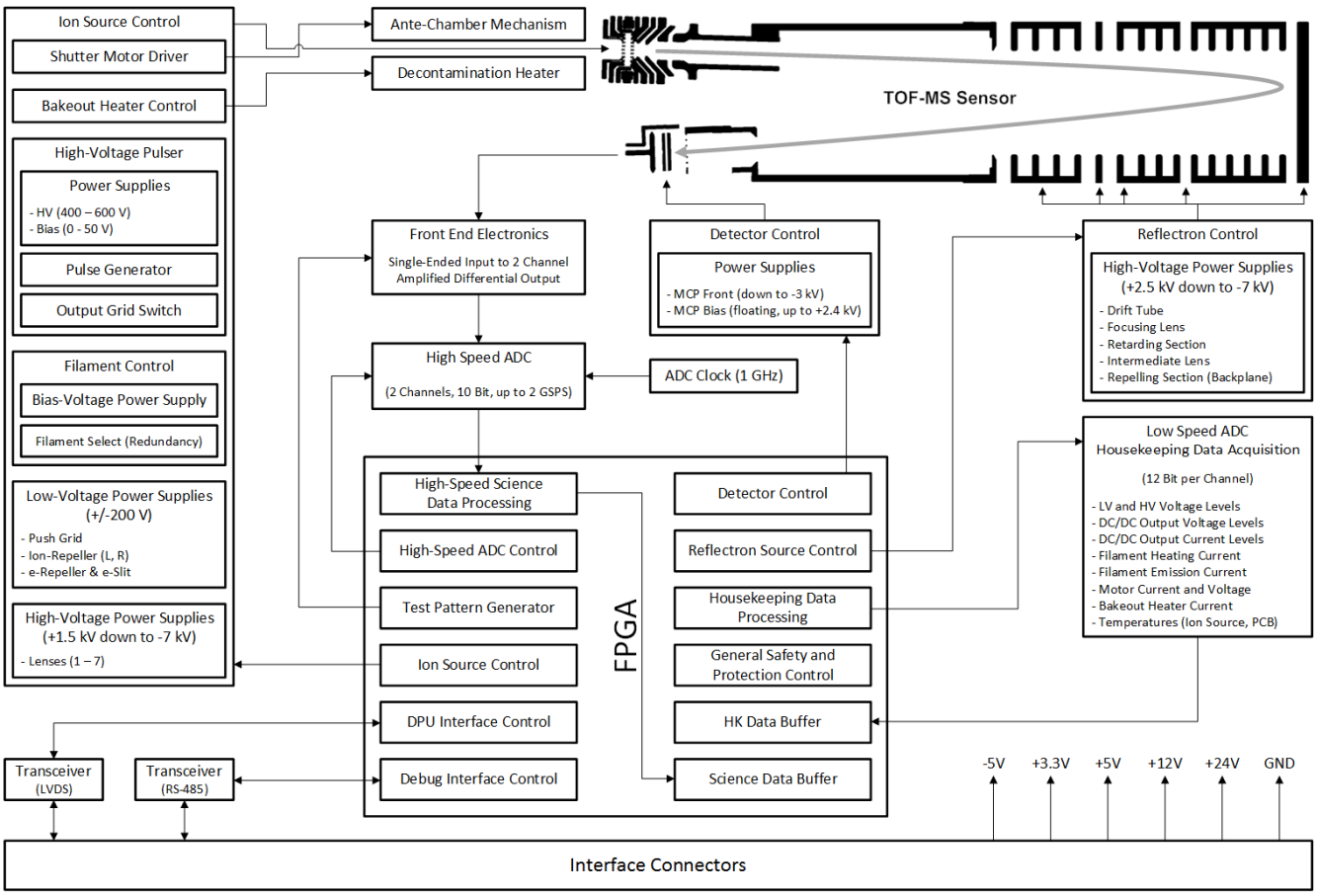

Figure 20 Block diagram of NIM's flight electronics.

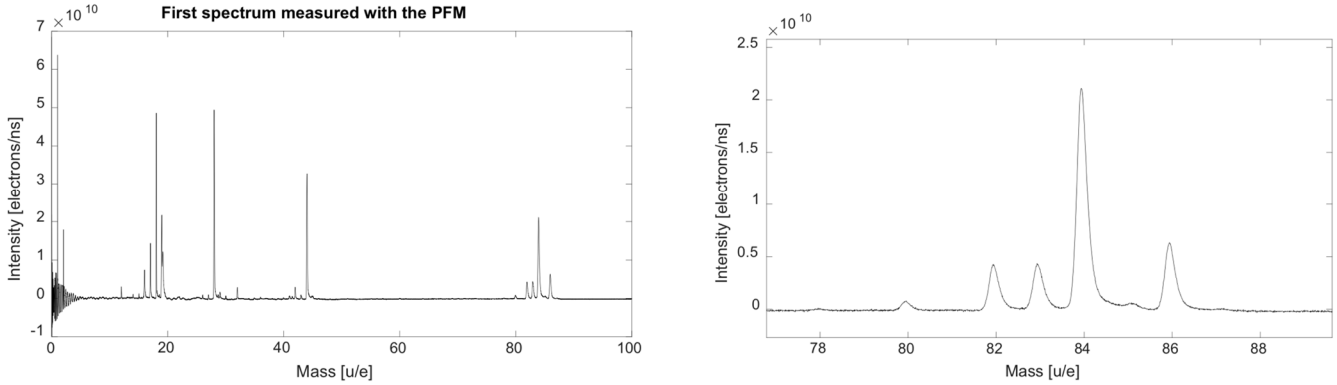

Figure 21 First spectrum measured with the PFM in residual gas mode; full spectrum to the left and zoom-in on Kr isotopes to the right (residual gas pressure $1.5 \cdot 10^{-9}$ mbar, increased by leaking krypton gas into the chamber until reaching $4 \cdot 10^{-9}$ mbar). The spectrum is the result of the integration of 1 million waveforms. A background file recorded with emission current off is subtracted to compensate for the noise induced by the high voltage pulser.

CONCLUSIONS

In this paper, we retraced our path through the key decisions and trade-offs made in the design of a Time-of-Flight Mass Spectrometer for Jupiter's icy moons: the NIM instrument onboard ESA's JUICE mission. We described decisions defined at the outset of the project *(*which we called *'given' decisions*) that bound the solution space explored by the development team, as well as the *architectural* and *design decisions*, and their trade-offs, made in Phase B and C of the project. Throughout, we highlighted technical and programmatic factors affecting these decisions. Moreover, we discussed how a late-test failure during the flight-model vibration test exposed one 'given' decisions that, ex-post and perhaps even ex-ante, should have been done differently.

This account both connects the dots of previously published work and presents new results, including the first mass spectra acquired with the instrument. While this is necessarily a partial description of the instrument's design, history, and results, it does offer a perspective that no deep dive into the many thousand pages of project documentation could offer.

Figure 22 NIM sensor Proto-Flight Model before the start of qualification and calibration in mid-2019.

All in all, we believe that this paper offers a useful collection of ideas, concepts, lessons learned, and insights that can inform the decisions about the architecture and design of future similar instruments.

It is worth saying that all decisions that we made looked the 'right ones' ex-ante, while we strived to achieve the best outcomes 'thinking inside the box' given to us. Therefore, future teams developing similar instruments under different constraints, incentives, and risk appetites could as well opt for entirely different choices.

We trust that describing not only the design solutions that we implemented but also the alternatives that we traded off and dropped can encourage a broad exploration of the design space of future time-of-flight mass spectrometers. If this will lead to yet better instruments and science, the intent of this paper will have been met.

ACKNOWLEDGEMENTS

We acknowledge the contribution of the many people at the University of Bern whose experience and skills were essential for the success of this project. We also wish to thank H.R. Elsener of EMPA for the invaluable collaboration since Rosetta. Moreover, we acknowledge the contribution of the PEP team, which positively influenced aspects of the design of NIM; in particular: S. Karlsson (IRF), S. Jaskulek (JHU-APL), and S. Barabash (IRF). The thorough work of the reviewers is highly appreciated, as it was of significant help and guidance to improve this manuscript.

This project has been funded by the Swiss Space Office, via the ESA PRODEX Office, and the Swiss National Science Foundation.

REFERENCES

[1] Grasset, O., Dougherty, M. K., Coustenis, A., Bunce, E. J., Erd, C., Titov, D., ... & Hussmann, H. (2013). JUpiter ICy moons Explorer (JUICE): An ESA mission to orbit Ganymede and to characterize the Jupiter system. Planetary and Space Science, 78, 1-21.

[2] Barabash, S., Karlsson, S., Wieser, M., Brandt, P., Westlake, J., Mitchell, D., ... & Fränz, M. (2015, October). Radiation mitigation in the Particle Environment Package (PEP) sensors for the JUICE mission. In European Planetary Science Congress (Vol. 10).

[3] Balsiger, H., Altwegg, K., Bochsler, P., Eberhardt, P., Fischer, J., Graf, S., ... & Müller, J. (2007). Rosina–Rosetta orbiter spectrometer for ion and neutral analysis. Space Science Reviews, 128(1-4), 745-801.

[4] Abplanalp, D., Wurz, P., Huber, L., Leya, I., Kopp, E., Rohner, U., ... & Barabash, S. (2009). A neutral gas mass spectrometer to measure the chemical composition of the stratosphere. Advances in space research, 44(7), 870-878.

[5] Hofer, L., Wurz, P., Buch, A., Cabane, M., Coll, P., Coscia, D., ... & Tulej, M. (2015). Prototype of the gas chromatograph–mass spectrometer to investigate volatile species in the lunar soil for the Luna-Resurs mission. Planetary and space science, 111, 126-133.

[6] Fausch, R. G., Wurz, P., Tulej, M., Jost, J., Gubler, P., Gruber, M., ... & Gerber, T. (2018, March). Flight electronics of GC-mass spectrometer for investigation of volatiles in the lunar regolith. In 2018 IEEE Aerospace Conference (pp. 1-13). IEEE.

[7] Griin, E. (1992). F echtig, H., Hanner, MS, Kissel, J., Lindblad, B. A., Linkert, D., Linkert, G., Morfill, GE and Zook, HA, The Galileo Dust Detector. Space Sci. Rec, 60, 317-340.

[8] Brockwell, T. G., Meech, K. J., Pickens, K., Waite, J. H., Miller, G., Roberts, J., ... & Wilson, P. (2016, March). The mass spectrometer for planetary exploration (MASPEX). In 2016 IEEE Aerospace Conference (pp. 1-17). IEEE.

[9] Vorburger, A., Pfleger, M., Lindkvist, J., Holmström, M., Lammer, H., Lichtenegger, H. I., ... & Wurz, P. (2019). 3D□modeling of Callisto's Surface Sputtered Exosphere Environment. Journal of Geophysical Research: Space Physics.

[10] Vorburger, A., & Wurz, P. (2018). Europa's ice-related atmosphere: The sputter contribution. Icarus, 311, 135-145.

[11] Plainaki, C., Cassidy, T. A., Shematovich, V. I., Milillo, A., Wurz, P., Vorburger, A., ... & Brandt, P. C. (2018). Towards a global unified model of Europa's tenuous atmosphere. Space science reviews, 214(1), 40.

[12] Miller, R., & Lessard, D. R. (2001). The strategic management of large engineering projects: Shaping institutions, risks, and governance. MIT press.

[13] Crawley, E., Cameron, B., & Selva, D. (2015). System architecture: strategy and product development for complex systems. Prentice Hall Press.

[14] Miller, G. A. (1956). The magical number seven, plus or minus two: Some limits on our capacity for processing information. Psychological review, 63(2), 81.

[15] Scherer, S., Altwegg, K., Balsiger, H., Fischer, J., Jäckel, A., Korth, A., ... & Wurz, P. (2006). A novel principle for an ion mirror design in time-of-flight mass spectrometry. International Journal of Mass Spectrometry, 251(1), 73-81.

[16] Lasi, D., Tulej, M., Neuland, M. B., Wurz, P., Carzaniga, T. S., Nesteruk, K. P., ... & Elsener, H. R. (2017, July). Testing the radiation hardness of thick-film resistors for a time-of-flight mass spectrometer at jupiter with 18 MeV protons. In 2017 IEEE Radiation Effects Data Workshop (REDW) (pp. 1-9). IEEE..

[17] Agostinelli, S., Allison, J., Amako, K. A., Apostolakis, J., Araujo, H., Arce, P., ... & Behner, F. (2003). GEANT4—a simulation toolkit. Nuclear instruments and methods in physics research section A: Accelerators, Spectrometers, Detectors and Associated Equipment, 506(3), 250-303.

[18] Karlsson, S. (2016, June). PEP radiation modelling report (PA-06.01). Rep. JUI- IRF-PEP-RP-002 v1.0.

[19] Desorgher, L. (2010, March). Radiation simulation study for the PEP-NU on the LAPLACE mission. SpaceIT GmbH, Bern, Switzerland, Rep. JGO- PEP-TN-0901 v1.0.

[20] Tulej, M., Meyer, S., Lüthi, M., Lasi, D., Galli, A., Desorgher, L., ... & Wurz, P. (2015). Detection efficiency of microchannel plates for e− and π− in the momentum range from 17.5 to 345 MeV/c. Review of scientific instruments, 86(8), 083310.

[21] Tulej, M., Meyer, S., Lüthi, M., Lasi, D., Galli, A., Piazza, D., ... & Kalla, L. (2016). Experimental investigation of the radiation shielding efficiency of a MCP detector in the radiation environment near Jupiter's moon Europa. Nuclear Instruments and Methods in Physics Research Section B: Beam Interactions with Materials and Atoms, 383, 21-37.

[22] Lasi, D., Tulej, M., Meyer, S., Lüthi, M., Galli, A., Piazza, D., ... & Hajdas, W. (2016). Shielding an MCP detector for a space-borne mass spectrometer against the harsh radiation environment in Jupiter's magnetosphere. IEEE transactions on nuclear science, 64(1), 605-613.

[23] Spencer, N. W., & Carignan, G. R. (1988). In situ measurements of thermospheric composition, temperature and winds by mass spectrometry. Adv. Space Res. Vol. 8, No. 5–6, pp (5)107–(5)117.

[24] Niemann, H. B., Booth, J. R., Cooley, J. E., Hartle, R. E., Kasprzak, W. T., Spencer, N. W., ... & Carignan, G. R. (1980). Pioneer Venus orbiter neutral gas mass spectrometer experiment. IEEE Transactions on Geoscience and Remote Sensing, (1), 60-65.

[25] Mahaffy, P. R., Benna, M., King, T., Harpold, D. N., Arvey, R., Barciniak, M., ... & Johnson, C. S. (2015). The neutral gas and ion mass spectrometer on the Mars atmosphere and volatile evolution mission. Space Science Reviews, 195(1-4), 49-73.

[26] Meyer, S., Tulej, M., & Wurz, P. (2017). Mass spectrometry of planetary exospheres at high relative velocity: direct comparison of open-and closed source measurements. Geoscientific instrumentation, methods and data systems, 6(1), 1-8.
[27] Curtis, C. C., & Hsieh, K. C. (1986). Spacecraft mass spectrometer ion source employing field emission cathodes. Review of Scientific Instr., 57(5), 989-990.
[28] Spindt, C. A. (1968). A thin-film field-emission cathode. Journal of Applied Physics, 39(7), 3504-3505.
[29] Tsujino, S., Beaud, P., Kirk, E., Vogel, T., Sehr, H., Gobrecht, J., & Wrulich, A. (2008). Ultrafast electron emission from metallic nanotip arrays induced by near infrared femtosecond laser pulses. Applied Physics Letters, 92(19), 193501.
[30] Zhang, H., Li, D., Wurz, P., Cheng, Y., Wang, Y., Wang, C., ... & Fausch, R. G. (2019). Residual Gas Adsorption and Desorption in the Field Emission of Titanium-Coated Carbon Nanotubes. Materials, 12(18), 2937.
[31] Curtis, C. C., Fan, C. Y., Hsieh, K. C., Hunten, D. M., Ip, W. H., Keppler, E., ... & Erö, J. (1988). Comet P/Halley neutral gas density profile along the Vega-1 trajectory measured by the Neutral Gas Experiment. In Exploration of Halley's Comet (pp. 360-362). Springer, Berlin, Heidelberg.
[32] Anguero, V. M., & Adamo, R. C. (1998, November). Space applications of spindt cathode field emission arrays. In 6th Spacecraft Charging Technology (pp. 347-352).
[33] Managadze, G. G., Wurz, P., Sagdeev, R. Z., Chumikov, A. E., Tuley, M., Yakovleva, M., ... & Bondarenko, A. L. (2010). Study of the main geochemical characteristics of Phobos' regolith using laser time-of-flight mass spectrometry. Solar System Research, 44(5), 376-384.
[34] Mesa, J. L., Fernández, A. B., Hernando, C., McHenry, M. E., Aroca, C., Alvarez, M. T., & Diaz-Michelena, M. (2014, July). Effects of gamma-ray radiation on magnetic properties of NdFeB and SmCo permanent magnets for space applications. In 2014 IEEE Radiation Effects Data Workshop (REDW) (pp. 1-4). IEEE.
[35] Elsener, H.R., Rheingans, B., Jeurgens, L.P.H., Burgdorf, T., Brüngger, S., Piazza, D., & Wurz, P (2019, May). Brazed metal-ceramic components for space applications. In Proceedings of the 12th International Conference on Brazing, High Temperature Brazing and Diffusion Bonding. DVS-Berichte 353, 207-214. Aachen, Germany.
[36] Bieler, A., Altwegg, K., Hofer, L., Jäckel, A., Riedo, A., Sémon, T., ... & Wurz, P. (2011). Optimization of mass spectrometers using the adaptive particle swarm algorithm. Journal of mass spectrometry, 46(11), 1143-1151.
[37] Graf, S., Altwegg, K., Balsiger, H., Jäckel, A., Kopp, E., Langer, U., ... & Wurz, P. (2004). A cometary neutral gas simulator for gas dynamic sensor and mass spectrometer calibration. Journal of Geophysical Research: Planets, 109(E7).

BIOGRAPHY

Davide Lasi *received a B.Sc. and an M.Sc. in Chemistry from the University of Milano in 2004 and 2006, and an M.S. from MIT in 2018 (System Design and Management). He has been with the University of Bern since 2011, as project manager for the development of three space mass spectrometers, including NIM for JUICE.*

Stefan Meyer *received a Ph.D. in Physics from the University of Bern in 2017, leading the development of NIM ion optics design. Since 2018, he works as Hearing Research Physicist at Bern University Hospital. Prior, he worked as a hardware engineer at RUAG Electronics. He received a B.A. in Electronics Engineering from University of Applied Sciences HTA Biel, Switzerland in 2003.*

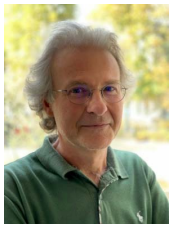

Daniele Piazza *has more than 20 years of experience in the design and development of space instruments. He has a Ph.D. in mechanical engineering from ETH Zurich and started his career in Formula 1. Since 2005 he leads the mechanical engineering group working on space instruments at the University of Bern.*

Matthias Lüthi *holds an M.Sc. from ETH, Zürich (1996) and an EMBA in management of technology from HEC Lausanne (2009). He has more than 20 years of experience as a hardware design engineer and manager in high-tech industries in the US and Switzerland. He is the NIM electronics systems engineer.*

Andreas Nentwig *received a B.Sc. and M.Sc. in Engineering from Bern University of Applied Sciences, specializing in electrical energy technologies and environment. After working for a Swiss company as Project Manager and Engineer for RF & Microwaves systems, he has been analog hardware engineer for NIM.*

Mario Gruber *received a B.Sc. in Computer Science from Bern University of Applied Sciences in 2008. At the University of Bern, he has been responsible for flight and ground software of LASMA and NGMS for Luna and NIM for JUICE mass spectrometers, and he has contributed to the success of CaSSIS on ExoMars' Trace Gas Orbiter.*

Stefan Brüngger *received a B.Sc. in Mechanical Engineering from Bern University of Applied Sciences in 2007. Since 2017, he is pursuing an M.Sc. in Systems Engineering Management at UCL (London). At the University of Bern, he worked as a mechanical design engineer for NIM on JUICE.*

Michael Gerber *has been employed as a systems engineer at the University of Bern since 2014, where he works on ExoMars Cassis and JUICE PEP. He graduated in mechanical engineering in 2006 and moved to the University of Bern from RUAG Aviation where he was a systems engineer on fighter aircraft.*

Saverio Braccini *is a Professor of physics at the Laboratory for High Energy Physics of the University of Bern. He proposed the realization of an innovative medical cyclotron for radioisotope production and multi-disciplinary research at Bern University Hospital. He contributed to developing new accelerators, detectors, and experiments of CERN's LEP and LHC.*

Marek Tulej *received a Ph.D. in Physical Chemistry from the University of Basel in 1999. After his post-doctoral period at Paul Scherrer Institute, he joined in 2008 the University of Bern as an instrument scientist for space missions, including Phobos-Grunt, Marco Polo-R, Luna-Resurs, and JUICE.*

Martina Föhn *received an M. Sc. in physics from the University of Bern in 2017, with a thesis on the scattering properties of charge state conversion surfaces for space applications for the JUICE and the IMAP missions. She is now pursuing a Ph.D. in physics and is responsible for the calibration of NIM.*

Peter Wurz *has a degree in electronic engineering (1985), an M.Sc. and a Ph.D. in Physics from Technical University of Vienna (1990). He has been a post-doctoral researcher at Argonne National Laboratory. At the University of Bern since 1992, he is a Professor of physics and since 2015 head of the Space Science and Planetology division. He has been Co-I and PI for many science instruments for space missions of ESA, NASA, ISRO, Roscosmos, and JAXA. He is PI of NIM and Co-PI of PEP onboard JUICE.*